Low variability of authigenic 10Be/9Be across the Holocene Po plain parasequences reveals suitability of dating method for highstand deltaic deposits

Kishan Aherwar, Michal Šujan, Alessandro Amorosi, Bruno Campo, Andrej Chyba, Adam Tomašových, Barbara Rózsová, Team Aster, Régis Braucher

Quaternary Science Advances 15 (2024) 100201

Contents lists available at ScienceDirect

Quaternary Science Advances

journal homepage: www.sciencedirect.com/journal/quaternary-science-advances

Low variability of authigenic $^{10}Be/^{9}Be$ across the Holocene Po plain parasequences reveals suitability of dating method for highstand deltaic deposits

Kishan Aherwar [a,*], Michal Šujan [a,b], Alessandro Amorosi [c], Bruno Campo [c], Andrej Chyba [d], Adam Tomašových [e], Barbara Rózsová [a], Aster Team [f,1], Régis Braucher [f]

[a] Department of Geology and Paleontology, Faculty of Natural Sciences, Comenius University in Bratislava, Ilkovičova 6, 842 15, Bratislava, Slovakia
[b] Laboratory of Quaternary Research, State Research Institute Nature Research Centre, 2 Akademijos Str., LT-08412, Vilnius, Lithuania
[c] Department of Biological, Geological and Environmental Sciences, University of Bologna, Via Zamboni 67, 40126, Bologna, Italy
[d] Institute of Chemistry, Slovak Academy of Sciences, Dúbravská cesta 9, 845 38, Bratislava, Slovakia
[e] Earth Science Institute, Slovak Academy of Sciences, Dúbravská cesta 9, 845 38, Bratislava, Slovakia
[f] CEREGE, CNRS-IRD-Collège de France-INRAE, Aix-Marseille Univ., 13545, Aix-en-Provence, France

ARTICLE INFO

Keywords:
Authigenic $^{10}Be/^{9}Be$ dating
Geochronology
Provenance change
Cosmogenic nuclides
Paleoenvironments
Depositional processes

ABSTRACT

The authigenic $^{10}Be/^{9}Be$ dating method presents a valuable tool for reconstructing depositional chronologies in sedimentary environments, requiring only ubiquitous mud for sampling. Nevertheless, studies elucidating the variability of the $^{10}Be/^{9}Be$ record preserved in epicontinental successions are lacking, despite the essential nature of such knowledge for the application of authigenic $^{10}Be/^{9}Be$ in geochronology. In this study, we investigate the variability of measured natural $^{10}Be/^{9}Be$ ratios in sediment cores recovered from the Holocene Po River delta plain in Northern Italy, aiming to unveil the influence of changing sedimentary environments and provenance on the beryllium isotopic signature. We identified significant variations in the authigenic $^{10}Be/^{9}Be$ ratios across parasequences, which correlates with a provenance change from the Eastern Alps to the Po River. The observed variation would cause an age offset of ~1 Myr if unrecognized in a dated succession. Our analysis revealed consistent ratios between the delta plain (primarily represented by swamp) and delta front consisting of proximal prodelta facies, suggesting a prevalent riverine signature in the proximal prodelta, likely maintained by hyperpycnal flow deposition. Statistical assessments based on random sampling and bootstrapping highlighted the importance of a sample size of $n > 10$. Furthermore, a standard deviation of the observed variability indicates a necessity of an additional 9% uncertainty in authigenic $^{10}Be/^{9}Be$ dating studies if the sample size is smaller. Overall, our findings emphasize that the normal regressive highstand settings of a deltaic system maintain relatively stable beryllium isotopic fluxes, which are favourable for the authigenic $^{10}Be/^{9}Be$ dating application, if provenance changes are known.

1. Introduction

Deltaic sediments are seen as an excellent marker of relative sea level fluctuations and offers crucial insight into the interaction between the coast and sea level change (Patruno and Helland-Hansen, 2018; Pellegrini et al., 2020; Nienhuis et al., 2023). It's a well-established fact that much of hydrocarbon resources are trapped in deltaic deposits. A reliable geochronological method is required to understand and interpret deltaic sedimentation processes, and temporal changes of deltaic depositional systems, which appears in response to sea level fluctuation and climate change (Lin et al., 2023; Nienhuis et al., 2023). In this study we explore the potential of the $^{10}Be/^{9}Be$ isotopic ratio in authigenic oxyhydroxide sedimentary phase as a robust dating technique for the highstand normal regressive delta deposits.

The authigenic $^{10}Be/^{9}Be$ technique has emerged as a novel chronometer in the recent decades. It is based on the radiogenic decay of an

* Corresponding author.
E-mail addresses: aherwar1@uniba.sk (K. Aherwar), michal.sujan@gamtc.lt (M. Šujan), alessandro.amorosi@unibo.it (A. Amorosi), Andrej.chyba@savba.sk (A. Chyba), adam.tomasovych@savba.sk (A. Tomašových), braucher@cerege.fr (R. Braucher).
[1] Aster Team: G. Aumaître, K. Keddadouche, F. Zaïdi.

https://doi.org/10.1016/j.qsa.2024.100201
Received 6 May 2024; Received in revised form 29 May 2024; Accepted 30 May 2024
Available online 31 May 2024

initial $^{10}Be/^{9}Be$ ratio to determine depositional ages of sediments in which the present $^{10}Be/^{9}Be$ ratio is measured (Bourlès et al., 1989). Up to the present-day, only a handful of studies have described the application of the method in the epicontinental basin settings (Barg et al., 1997; Sapota et al., 2006; Lebatard et al., 2008, 2010; McHargue et al., 2011; Schaller et al., 2015; Šujan et al., 2016, 2020, 2023a, 2023b; Botka et al., 2019; Magyar et al., 2019; Lisé-Pronovost et al., 2021; Jeong et al., 2023). This is strongly related to the fact that the factors influencing the dating technique remain insufficiently researched. Since the stable isotope ^{9}Be is generated by the weathering of rocks and atmospheric ^{10}Be is a cosmogenic radionuclide, the distinct sources of the two isotopes leads in a shifting $^{10}Be/^{9}Be$ ratio from deltaic to offshore settings (Wittmann et al., 2017; Kong et al., 2021). Detailed authigenic $^{10}Be/^{9}Be$ profiles through deltaic parasequences by Graham et al. (1998) have suggested that flooding periods at the parasequence boundaries may be accompanied by a major ^{9}Be delivery decrease. Apart from the riverine input of dissolved ^{9}Be, recent research points to the diagenetic release of beryllium as another factor increasing the complexity of the system (Deng et al., 2023). Nonetheless, the variation of the initial $^{10}Be/^{9}Be$ across different parts of the deltaic environment remains critically unexplored, despite being an essential knowledge for the robust use of the method in such settings.

In this study, we present the variation in the measured natural authigenic $^{10}Be/^{9}Be$ ratio from five boreholes recovered in the modern Po River delta plain (Northern Italy, Fig. 1). The Po delta renowned for its wealth of available data, represents an ideal investigation site. Recent studies (Amorosi et al., 2017; Bruno et al., 2017) based on sedimentological, stratigraphic, paleontological and geotechnical data, have subdivided the Holocene sedimentary succession into eight parasequences (*sensu* Van Wagoner et al., 1988; Van Wagoner et al., 1990) within a very high-resolution radiocarbon-dated chronological framework. Stratigraphic architecture reconstruction was additionally integrated by bulk-sediment geochemistry and benthic foraminiferal analyses that led to an accurate reconstruction of the Po Plain deltaic succession in terms of sediment provenance, clinothem boundaries identification and progradational dynamics of coastal systems (Greggio et al., 2018; Amorosi et al., 2019, 2020). Based on this exceptional dataset, 50 samples representative of deltaic environments have been specifically collected and analyzed within this study from cores EM 5, EM 8, EM 9, EM 10, and EM 13 (Fig. 1C for location). An observed change in sediment source within the sampled depositional record as reported by Amorosi et al. (2020) provides us an opportunity to investigate the effect of provenance change on the authigenic $^{10}Be/^{9}Be$ ratio as our Hypothesis 1. The wide range of sampled environments spanning swamp, poorly drained floodplain, lagoon, proximal prodelta, and distal prodelta to inner shelf allows to validate the Hypothesis 2 regarding the influence of different

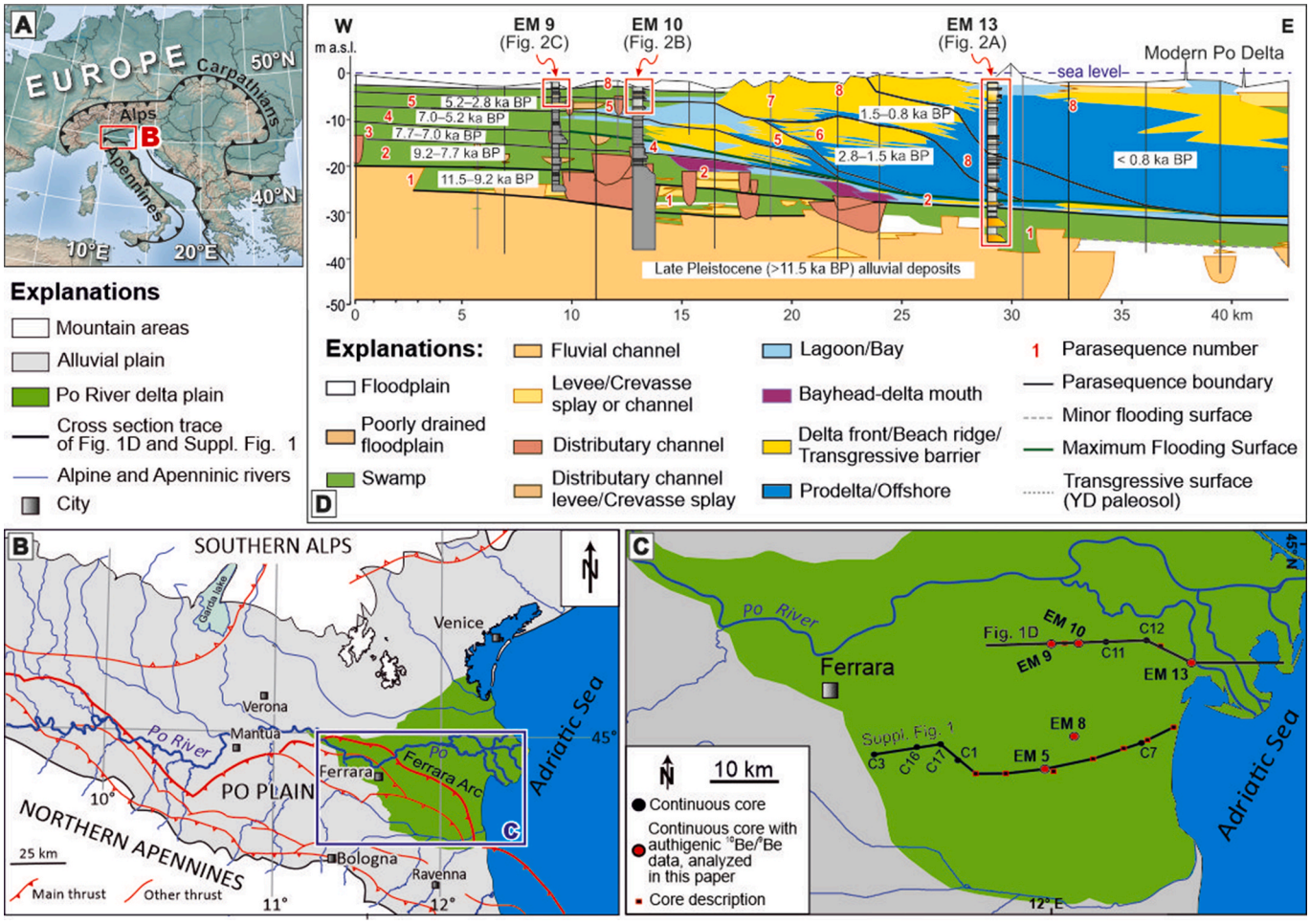

Fig. 1. (A) Location of the eastern Po Basin, (B) Po Plain and the present-day river network supplying the deltaic system from Southern Alps and Northern Apennines, (C) a detailed view on the Po Plain with location of the studied well-cores, (D) a schematic geological section illustrating stratal architecture through the Holocene succession of the Po coastal plain according to Amorosi et al. (2017). A detailed version of the correlation panel including sedimentological and stratigraphic data supporting the correlation is included in Suppl. Fig. 1. Location in Fig. 1C. Three of the five analyzed well-cores are depicted. Well-cores EM 5 and EM 8 are shown in Suppl. Fig. S1.

paleoenvironmental settings, including sediment source proximity, mixing of riverine and basinal waters, depositional and post-depositional processes on the authigenic $^{10}Be/^{9}Be$. The well-constrained Holocene age (younger than 7.0 cal ka BP) of the sampled strata renders the ^{10}Be radioactive decay irrelevant, enabling the interpretation of changes in authigenic $^{10}Be/^{9}Be$ solely as the result of paleoenvironmental changes.

The objective of this study is to elucidate the predictability of the authigenic $^{10}Be/^{9}Be$ variability in the depositional record of normal regressive deltaic deposits accumulated in highstand settings and, thereby, to introduce the potential of authigenic $^{10}Be/^{9}Be$ method. The study emphasizes the limitations and cautions in sampling that must be considered, along with the necessity of sedimentological and provenance analysis while applying this method. Special attention is given to the implications of the authigenic $^{10}Be/^{9}Be$ variability on dating uncertainty, which is essential for reliable geochronology.

2. Geological settings

The Po River basin (Fig. 1A) is a foreland basin system framed between the south-verging Southern Alps and the north-verging Apennines (Burrato et al., 2003). Its formation is linked to the convergence between the Adria microplate and the European Plate since the Cretaceous (Carminati and Doglioni, 2012). Whereas the south Alpine buried structures consist of a single arc-shaped thrust system with a W-E direction (Vannoli et al., 2015), the Northern Apennines front includes a more complex arched thrust system (Fig. 1B), active since the Late Miocene (Picotti and Pazzaglia, 2008; Boccaletti et al., 2011). These latter structures are buried beneath the Plio-Quaternary sedimentary infill of the Po Basin, up to 8 km-thick in the depocenters, and characterized by an overall shallowing-upward trend from older marine to younger alluvial deposits (Pieri and Groppi, 1981; Ori, 1993). The study area is located in the eastern sector of the southern Po Plain, south the modern Po River (Fig. 1B and C) and coincides with the modern Po Delta plain (Fig. 1C). In this sector, Holocene deposits form a peculiar transgressive-regressive (T-R) sedimentary wedge composed of coastal to shallow-marine facies associations overlying late Pleistocene alluvial strata (Fig. 1D, Supplementary Fig. S1).

The T-R wedge has been subdivided into eight millennial-scale parasequences (Fig. 1D, Supplementary Fig. S1 – after Amorosi et al., 2017). Parasequences 1 to 3 (11.5–7.0 cal ka BP, Fig. 1D) include early Holocene estuarine deposits and show a retrogradational stacking pattern (Fig. 1D) that reflects the post-glacial stepwise sea-level rise (Amorosi et al., 2017). In the study area, estuarine strata are strongly dominated by muddy facies such as freshwater poorly-drained floodplain and organic-rich swamp deposits, and brackish lagoonal clays (Bruno et al., 2017). Downdip, estuarine deposits are transitional to nearshore (transgressive barrier sands) and shallow-marine (i.e., offshore) muds (Fig. 1D). Parasequence 3 records the maximum landward migration of the shoreline linked to the last phase of sea-level rise and following sea-level stabilization (Amorosi et al., 2017), and the establishment of estuarine conditions with a bay-head delta progradational system fed by the Po River (Amorosi et al., 2019). Parasequences 4 to 8 (7.0 cal ka BP to Present) are characterized by middle to late Holocene coastal-deltaic facies stacked in aggradational to progradational pattern (Fig. 1D), recording the multi-phase Po delta upbuilding with repeated activation and deactivation episodes of distributary-channels and delta-lobe switching (Correggiari et al., 2005; Amorosi et al., 2019). The dominantly autogenic delta architecture of parasequences 4 to 8 is genetically related to the rapidly deposited mud wedge characterizing the Western Adriatic shelf for about 600 km along the Italian coast (Cattaneo et al., 2003, 2007). The aggradational parasequences 4 to 6 (7.0–2.0 cal ka BP, Fig. 1D) reflect the development of a shallow, wave-dominated coastal system with modestly crescent and elongated beach deposits (Amorosi et al., 2019). In this phase, the study area was characterized by weak progradation and development of E-dipping clinothems nourished by the Po River at proximal and southern locations (Amorosi et al., 2020, see parasequences 4 to 5 in cores 204S3, EM 5 and EM 11 of their Fig. 5), as suggested by available bulk sediment geochemical data. Seawards, the distal segments of these clinothems were preferentially fed by sediment with high MgO/Al_2O_3 (and low Cr/Al_2O_3) levels, and suggesting limestone and dolostone-rich Eastern Alps catchments as the prevalent sediment source via south-directed longshore currents (Amorosi et al., 2020). A dominant Alpine sediment contribution, with only subordinate Po component, is recorded by parasequence 6. Parasequences 7 and 8 (last 2.0 ka BP) document the faster accretion of the rapidly prograding delta lobes and the transition to a river-dominated system fed by the Po River, as suggested by very high Cr/Al_2O_3 and low MgO/Al_2O_3 ratio, very similar to modern Po River sediments (Amorosi et al., 2019, 2020). The prominent shift in sediment composition from Alpine (parasequence 6) to Po River (parasequence 7) contribution is linked to the activation of the *Po di Volano* branch that marked the replacement of the S-directed Mg-rich (Alpine) sediment supply with sediment from the prograding Po Delta lobes (Amorosi et al., 2019, 2020). Beneath the modern shoreline of the study area, in along-strike direction, above transgressive sands and offshore clays, the regressive unit is up to 30 m-thick, with prodelta muds overlain by laterally continuous (>60 km) beach-ridge/delta front sands of the modern delta plain (Campo et al., 2017).

3. Methods

3.1. Principles of the authigenic $^{10}Be/^{9}Be$ dating

The authigenic $^{10}Be/^{9}Be$ dating method uses the decay of atmospheric cosmogenic radionuclide ^{10}Be to determine the depositional ages of sediment in the age range of 0.2 Ma to 14 Ma, owing to 1.387 ± 0.01 Ma half-life of ^{10}Be (Chmeleff et al., 2010; Korschinek et al., 2010). The stable isotope ^{9}Be originates from erosion of rock massifs, decomposition of primary minerals by chemical weathering, and gets dissolved in the water column of the hydrosphere (Measures and Edmond, 1983; Brown et al., 1992). The cosmogenic nuclide ^{10}Be is produced in atmosphere through spallation reaction by interaction of cosmic rays with nitrogen and oxygen and is transferred to the Earth surface primarily by precipitation (Raisbeck et al., 1981). Both isotopes get incorporated into the oxyhydroxides of Fe and Mn, which are the main carrier of Be isotopes deposited in authigenic phase (Bourlès et al., 1989; Willenbring and von Blanckenburg, 2010; Wittmann et al., 2012; Singleton et al., 2017). The temporal change in the $^{10}Be/^{9}Be$ ratio within the authigenic rims around the surface of sedimentary particles is proportional to the depositional age of a bed due to the radioactive decay of ^{10}Be, provided that the system remains chemically closed (with beryllium loss occurring solely due to the decay of ^{10}Be).

The radioactive decay equation, $R = R_0 \times e^{-\lambda t}$, where R is the measured isotopic $^{10}Be/^{9}Be$ ratio, R_0 denotes the initial isotopic ratio, λ the decay constant of ^{10}Be, and t the time elapsed since deposition, serves as the basis for determining the age of the deposited sediment. However, a precise determination of the initial authigenic ratio R_0 is an essential requirement for application of the method (Lebatard et al., 2008, 2010; Šujan et al., 2016, 2020, 2023a). Two viable options for resolving R_0 include analysis of recent or independently dated equivalents of the facies to be dated with authigenic $^{10}Be/^{9}Be$.

Von Blanckenburg et al. (2012) suggest that changes in ^{9}Be delivery dependent on variation in catchment lithology are averaged in large river catchments such as Amazon, while contrasting petrography of smaller catchments diverging significantly from the average crustal composition will yield various amounts of ^{9}Be. The influence of catchment petrography on the ^{9}Be supply to the authigenic phase was declared by Rahaman et al. (2017) and Dannhaus et al. (2018). The state-of-the-art knowledge further underscores the importance of considering temporal changes in depositional rates, denudation rates, depositional and post-depositional processes, sediment source proximity

and potential redeposition of sediment when selecting an appropriate strategy for determining R_0 (Lebatard et al., 2008; von Blanckenburg and Bouchez, 2014; Wittmann et al., 2017; Dixon et al., 2018; Jeong et al., 2023; Šujan et al., 2023a, b). The described factors are prerequisites for the changes of authigenic $^{10}Be/^{9}Be$ from deltaic to offshore settings, as documented on the continental slope scale (Wittmann et al., 2017; Kong et al., 2021), yet remain unrecognized within a delta-scale system (*sensu* Patruno and Helland-Hansen, 2018; Pellegrini et al., 2020).

3.2. Hypotheses and sampling strategy

Sampling was carried out in accordance with the hypotheses outlined in this study: (1) that a change in sediment provenance within a river delta depositional system would influence the authigenic $^{10}Be/^{9}Be$ variability, and (2) that variations in depositional and post-depositional processes from the delta plain to the prodelta, associated with mixing of riverine and basinal waters, would impact the variability of authigenic $^{10}Be/^{9}Be$. As the method requires fine-grained sediment to achieve the highest reactive surface of the particles, only mud-dominated facies association (FA) were subject to sampling. Leveraging detailed facies analysis and architectural reconstructions within a high-resolution chronostratigraphic framework (comprising over 100 radiocarbon dates – see Amorosi et al., 2017, 2019; Bruno et al., 2017 among others), fifty samples were collected from cores EM 5, EM 8, EM 9, EM 10, and EM 13 (Figs. 1 and 2), additional information on facies characterization are provided in the Supplementary Table S1. Among these 50 samples, 30 samples were picked up from the borehole EM 13 (parasequences 6, 7, and 8) which include distal prodelta, proximal prodelta, and inner shelf to prodelta FAs. The vertical succession of samples within the EM 13 core includes a transition in provenance from the Northern Alpine rivers in the parasequence 6 to the Po River in the parasequences 7 and 8 (Amorosi et al., 2020), thereby enabling the examination of the impact of changing sediment source on the authigenic $^{10}Be/^{9}Be$ record (Hypothesis 1). Importantly, this shift in provenance occurred while maintaining the deposition within the proximal prodelta environment.

A 25 km long transect across all five cores encompasses a variety of FAs including swamp, poorly drained floodplain, lagoon, proximal and distal prodelta and inner shelf FA within the parasequences 5, 7, and 8, all with the same provenance (Amorosi et al., 2020) (Fig. 2). This collection of samples verifies Hypothesis 2, representing major sediment traps of mud in the wave-to river-dominated deltaic system (Pellegrini et al., 2021, 2023). More specifically, seven samples from EM 10 (parasequence 5 and 7) include lagoonal and freshwater swamp FAs. Core EM 9 (parasequence 5, 7 and 8) yielded seven samples comprising poorly drained floodplain and swamp deposits. Four samples from core EM 8 (parasequence 5 and 7) record a transition from lagoon to poorly drained floodplain FA. The remaining two samples were collected from core EM 5 (parasequence 7) representing swamp facies (Fig. 2). The parameters used for definition of analyzed FA are specified in Supplementary Table S1.

The sampling strategy was focused on the strata present deeper than 1 m below the surface (98% of the samples), and 84% of the samples are deeper than 2 m. It has a significant advantage for evaluation of the authigenic $^{10}Be/^{9}Be$ variation in depositional record in comparison to the sampling from present-day riverbed or suspended sediment (e.g., Rahaman et al., 2017; Dannhaus et al., 2018; Portenga et al., 2019). The sediment taken in the latter approach did not pass the pene-contemporaneous and secondary processes associated with early diagenesis, such as the pedogenesis on the alluvial and delta plain (Aslan and Autin, 1999; Campo et al., 2016) or benthic pore water cycling in the basinal environment (Middelburg et al., 1997), both of which are proven to significantly affect the beryllium isotopic inventories (Tsai et al., 2008; Graly et al., 2010; Willenbring and von Blanckenburg, 2010; Bacon et al., 2012; Dixon et al., 2018; Deng et al., 2023). Therefore, the employed sampling strategy enables the utilization of empirical observations to draw broader implications for the application of authigenic $^{10}Be/^{9}Be$ geochronology in significantly older sedimentary successions.

Singleton et al. (2017) indicated that meteoric ^{10}Be concentration in the authigenic phase is significantly correlated with the concentration of iron and manganese in soils of several alluvial basins across all analyzed grain sizes. On the other hand, cycling of Be in marine sediment porewater is driven by particulate supply and Mn–Fe cycling according to Deng et al. (2023). Hence, we aimed to focus on whether the Be isotopic ratio could be affected by diagenetic release, and also the relation between pronounced meteoric ^{10}Be input on delta plain with more developed authigenic rims with higher Fe and Mn concentrations. Elemental concentrations of Fe, Mn and Al in the authigenic phase were analyzed for this purpose.

3.3. Sample processing and measurements

The method utilized for sample preparation in this study closely follows the protocol described by Šujan et al. (2024), which is based on the methodology of Bourlès et al. (1989) and Carcaillet et al. (2004). Sample preparation for both, accelerator mass spectrometry (AMS) and inductively coupled plasma-mass-spectrometry (ICP-MS) measurements was carried out at the laboratory of the Department of Geology and Paleontology, Faculty of Natural Sciences, Comenius University Bratislava (Slovakia). A total of 50 muddy samples were dried in oven at 70°C for 24 h and crushed to powder. An amount of ~2.25 g crushed sample was mixed with leaching solution (0.04 M NH_2OH–HCl in 25% acetic acid) and left in magnetic stirrer for 7 h at ~95 °C to extract the authigenic phase. The leaching solution used in sample processing, extracts the authigenic phase adsorbed on the surface of the sediment, which consists of oxyhydroxides of iron and manganese and is considered as the main carrier of beryllium isotopes (Wittmann et al., 2012). An aliquot of ~2 ml was separated from the leached solution to perform ICP-MS measurement for determining the concentration of ^{9}Be and elements Fe, Mn, and Al, as the principal components of the authigenic phase. A linear regression method was applied in the case of ^{9}Be ICP-MS measurement to mitigate the matrix effect (Tan and Horlick, 1987) and to minimize the uncertainty.

The remaining fraction of the leached solution was spiked with ~450 μl of ^{9}Be ICP-MS commercial standard from LGC having $^{10}Be/^{9}Be$ ratio measured two times to reach 3.42×10^{-15} to 3.61×10^{-15} and a Be concentration of 1000 ppm. The spiked solution was then evaporated and purified with column chromatography to separate beryllium from other elements (Merchel and Herpers, 1999). The resulting precipitate was washed and left with pH 8–9 water overnight for aging (Merchel et al., 2019). Further steps included dissolution of precipitate in HNO_3 and evaporation, followed by oxidizing the sample at 800 °C for 1 h. BeO powder thus obtained was mixed with niobium powder to prepare the cathodes for AMS measurement.

The elemental concentration of ^{9}Be, Fe, Mn, and Al was measured using the PlasmaQuant ICP-MS System (Analytik Jena AG) facility at the Institute of Chemistry, Slovak Academy of Sciences. Isotopic $^{10}Be/^{9}Be$ ratio measurement was performed at the French National AMS Facility ASTER, CEREGE, Aix-en-Provence (France). The measured isotopic ratios at AMS were corrected by corresponding chemical processing blank's isotopic ratio with one blank for each seven samples. The seven blanks reached $^{10}Be/^{9}Be$ isotopic ratios in the range of 5.08×10^{-15} to 9.24×10^{-15}, three orders of magnitude lower than AMS ratio measured in the samples. The measurements were calibrated directly against the STD11 in-house standard ($^{10}Be/^{9}Be$ value of $(1.191 \pm 0.013) \times 10^{-11}$) (Braucher et al., 2015). Analytical uncertainties (reported as 1σ) include uncertainties associated with AMS counting statistics, chemical blanks correction and the AMS internal error (0.5%).

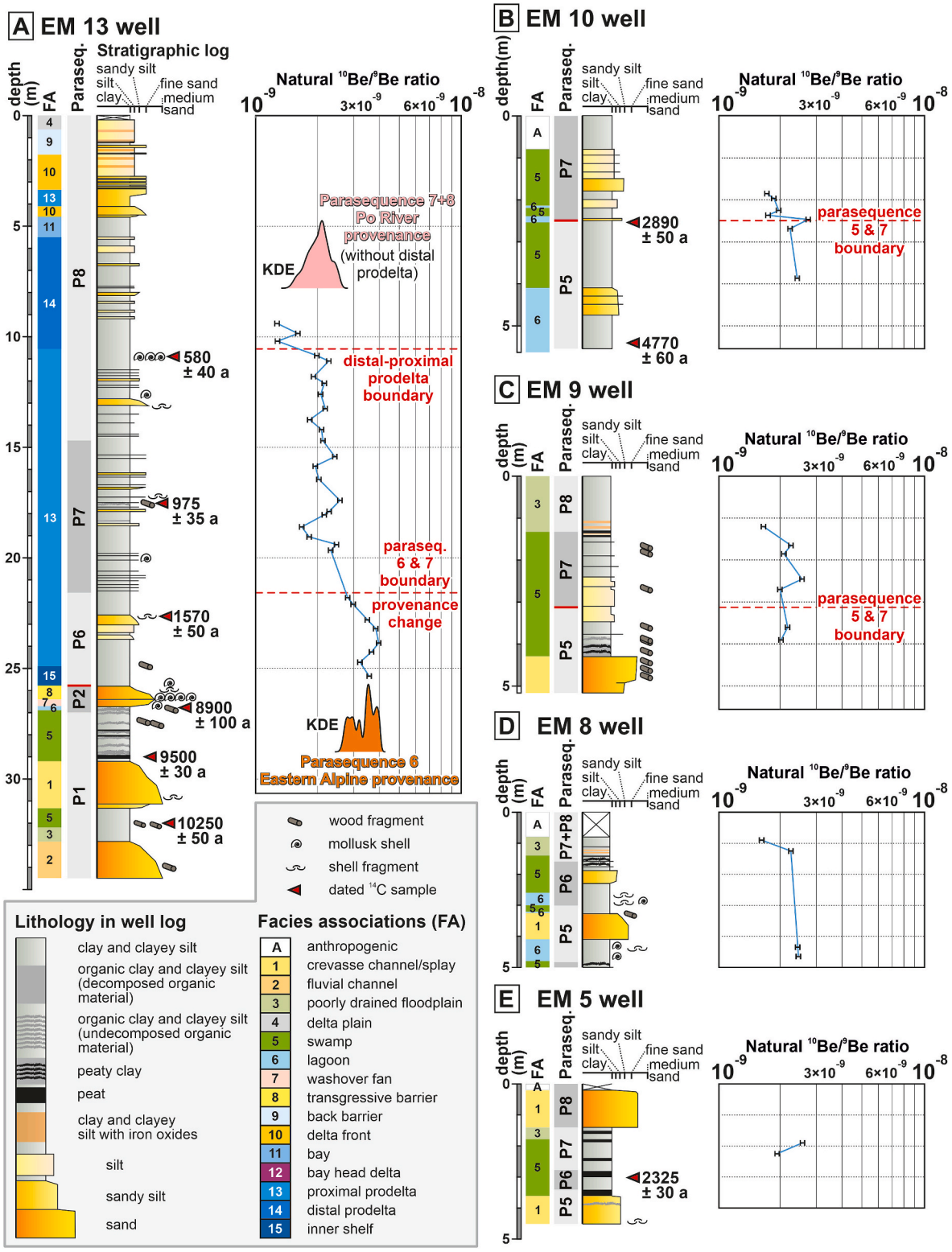

Fig. 2. Variation of the measured natural $^{10}Be/^{9}Be$ across 5 different boreholes for all 50 samples, KDE plots are also visualized based on Spencer et al. (2017) for borehole EM 13, as it was sampled for maximum number of samples (30) from three different parasequences 6,7 and 8 (excluding distal prodelta samples from parasequence 8). Note the logarithmic scale on the horizontal axis with $^{10}Be/^{9}Be$ values. Sedimentological profiles of the boreholes, classification of facies associations, prasequence numbers and calibrated radiocarbon ages are based on Amorosi et al. (2017, 2019). Location of the boreholes in Fig. 1C. KDE – Kernel density estimation.

Table 1
Concentrations of ^{9}Be and ^{10}Be, $^{10}Be/^{9}Be$ ratios measured by accelerator mass spectrometry (AMS) and calculated natural $^{10}Be/^{9}Be$ ratios for the samples of Po Delta plain parasequences. Reported uncertainties are 1σ. Concentrations of ^{10}Be are corrected to the $^{10}Be/^{9}Be$ ratios of seven processing blanks reaching values in the range of 5.08×10^{-15} to 9.24×10^{-15}. Sample ID consist of the borehole name (e.g., "EM 5") and the depth of sampling in meters below the terrain (e.g., 1.9). Facies association classification is based on Amorosi et al. (2017, 2019). Abbreviations: PDF – poorly drained floodplain, IStP – inner shelf to prodelta.

Sample ID	Facies association	Paraseq. Nr.	^{9}Be (at $\times g^{-1}$) $\times 10^{16}$	AMS $^{10}Be/^{9}Be$ ($\times 10^{-12}$)	^{10}Be (at $\times g^{-1}$) $\times 10^{8}$	Natural $^{10}Be/^{9}Be$ ($\times 10^{-9}$)
EM 5–1.9	Swamp	7	7.74 ± 0.15	6.54 ± 0.32	1.98 ± 0.02	2.56 ± 0.06
EM 5–2.25	Swamp	7	7.04 ± 0.14	4.48 ± 0.22	1.36 ± 0.02	1.92 ± 0.04
EM 8–0.9	PDF	7	4.97 ± 0.09	2.67 ± 0.13	0.80 ± 0.01	1.62 ± 0.04
EM 8–1.25	PDF	7	15.62 ± 0.31	1.15 ± 0.57	3.15 ± 0.04	2.25 ± 0.05
EM 8–4.35	Lagoon	5	5.38 ± 0.10	4.32 ± 0.21	1.30 ± 0.01	2.42 ± 0.06
EM 8–4.65	Lagoon	5	5.53 ± 0.11	4.48 ± 0.22	1.35 ± 0.002	2.44 ± 0.06
EM 9–1.2	PDF	8	11.47 ± 0.22	6.24 ± 0.31	1.89 ± 0.02	1.65 ± 0.04
EM 9–1.65	Swamp	7	6.97 ± 0.13	5.18 ± 0.25	1.56 ± 0.02	2.24 ± 0.05
EM 9–1.85	Swamp	7	6.93 ± 0.13	4.77 ± 0.23	1.44 ± 0.02	2.07 ± 0.05
EM 9–2.45	Swamp	7	7.17 ± 0.14	6.01 ± 0.30	1.82 ± 0.02	2.54 ± 0.06
EM 9–2.7	Swamp	7	7.20 ± 0.14	4.71 ± 0.23	1.43 ± 0.02	1.98 ± 0.04
EM 9–3.6	Swamp	5	8.04 ± 0.16	5.74 ± 0.28	1.73 ± 0.02	2.16 ± 0.05
EM 9–3.9	Swamp	5	7.55 ± 0.15	5.01 ± 0.25	1.52 ± 0.02	2.01 ± 0.05
EM 10–1.85	Swamp	7	6.36 ± 0.12	3.64 ± 0.18	1.10 ± 0.01	1.72 ± 0.04
EM 10–1.95	Swamp	7	5.98 ± 0.11	3.69 ± 0.18	1.11 ± 0.01	1.86 ± 0.04
EM 10–2.25	Swamp	7	5.38 ± 0.10	3.51 ± 0.17	1.06 ± 0.01	1.97 ± 0.04
EM 10–2.35	Swamp	7	6.24 ± 0.12	3.61 ± 0.18	1.09 ± 0.01	1.75 ± 0.04
EM 10–2.45	Lagoon	7	5.69 ± 0.11	5.17 ± 0.25	1.56 ± 0.02	2.74 ± 0.06
EM 10–2.67	Swamp	5	7.66 ± 0.15	5.67 ± 0.28	1.71 ± 0.02	2.23 ± 0.05
EM 10–3.85	Swamp	5	5.88 ± 0.11	4.74 ± 0.23	1.43 ± 0.02	2.42 ± 0.05
EM 13–9.4	Distal prodelta	8	7.42 ± 0.14	3.12 ± 0.15	0.94 ± 0.01	1.27 ± 0.03
EM 13–9.85	Distal prodelta	8	7.35 ± 0.14	3.92 ± 0.19	1.18 ± 0.01	1.61 ± 0.03
EM 13–10.2	Distal prodelta	8	7.26 ± 0.14	3.08 ± 0.15	0.92 ± 0.01	1.28 ± 0.03
EM 13–10.85	Distal prodelta	8	6.89 ± 0.13	4.54 ± 0.22	1.37 ± 0.02	1.99 ± 0.04
EM 13–11.1	Distal prodelta	8	6.36 ± 0.12	4.83 ± 0.24	1.44 ± 0.02	2.27 ± 0.05
EM 13–11.8	Proximal Prodelta	8	7.03 ± 0.14	4.46 ± 0.22	1.35 ± 0.01	1.91 ± 0.04
EM 13–12.1	Proximal Prodelta	8	5.26 ± 0.10	3.76 ± 0.18	1.14 ± 0.01	2.16 ± 0.05
EM 13–12.6	Proximal Prodelta	8	5.64 ± 0.11	3.87 ± 0.19	1.17 ± 0.01	2.07 ± 0.05
EM 13–13.25	Proximal Prodelta	8	6.96 ± 0.13	5.23 ± 0.26	1.52 ± 0.02	2.18 ± 0.05
EM 13–13.75	Proximal Prodelta	8	6.87 ± 0.13	4.17 ± 0.20	1.26 ± 0.01	1.84 ± 0.04
EM 13–14.2	Proximal Prodelta	8	5.45 ± 0.10	3.77 ± 0.18	1.14 ± 0.01	2.09 ± 0.05
EM 13–14.7	Proximal Prodelta	8	6.42 ± 0.12	4.52 ± 0.22	1.37 ± 0.01	2.13 ± 0.05
EM 13–15.42	Proximal Prodelta	7	5.84 ± 0.11	4.69 ± 0.23	1.42 ± 0.01	2.43 ± 0.05
EM 13–15.85	Proximal Prodelta	7	6.26 ± 0.12	4.05 ± 0.20	1.22 ± 0.01	1.95 ± 0.04
EM 13–16.45	Proximal Prodelta	7	6.79 ± 0.13	4.56 ± 0.22	1.38 ± 0.01	2.03 ± 0.04
EM 13–17.4	Proximal Prodelta	7	6.59 ± 0.13	5.60 ± 0.28	1.70 ± 0.02	2.57 ± 0.06
EM 13–17.9	Proximal Prodelta	7	7.28 ± 0.14	5.48 ± 0.27	1.66 ± 0.02	2.28 ± 0.05
EM 13–18.05	Proximal Prodelta	7	6.91 ± 0.13	4.93 ± 0.24	1.49 ± 0.02	2.16 ± 0.05
EM 13–18.6	Proximal Prodelta	7	7.09 ± 0.14	3.93 ± 0.19	1.19 ± 0.01	1.68 ± 0.04
EM 13–19.05	Proximal Prodelta	7	6.46 ± 0.12	3.91 ± 0.19	1.18 ± 0.01	1.82 ± 0.04
EM 13–19.4	Proximal Prodelta	7	6.41 ± 0.12	5.23 ± 0.26	1.59 ± 0.02	2.48 ± 0.06
EM 13–19.65	Proximal Prodelta	7	6.13 ± 0.12	4.68 ± 0.23	1.42 ± 0.02	2.32 ± 0.05
EM 13–21.8	Proximal Prodelta	7	4.78 ± 0.09	4.43 ± 0.22	1.34 ± 0.01	2.80 ± 0.06
EM 13–22.1	Proximal Prodelta	7	4.51 ± 0.09	4.44 ± 0.22	1.35 ± 0.02	2.98 ± 0.07
EM 13–22.8	Proximal Prodelta	6	4.05 ± 0.08	4.69 ± 0.23	1.42 ± 0.02	3.50 ± 0.08
EM 13–23.2	Proximal Prodelta	6	3.64 ± 0.07	4.60 ± 0.23	1.40 ± 0.02	3.84 ± 0.09
EM 13–23.85	Proximal Prodelta	6	3.78 ± 0.07	4.96 ± 0.24	1.50 ± 0.18	3.97 ± 0.49
EM 13–24.25	Proximal Prodelta	6	4.75 ± 0.09	5.73 ± 0.28	1.74 ± 0.02	3.66 ± 0.09
EM 13–24.75	Proximal Prodelta	6	5.57 ± 0.11	5.91 ± 0.29	1.79 ± 0.02	3.22 ± 0.07
EM 13–25.35	IStP	6	4.82 ± 0.09	5.66 ± 0.28	1.72 ± 0.02	3.57 ± 0.08

3.4. Random sampling and bootstrapping to estimate 95% CI

A statistical approach in R software (version 4.2.0) was employed to investigate the variability of initial authigenic $^{10}Be/^{9}Be$ ratio obtained in this study (for Holocene Po plain) as a function of sample size and to visualize how this variability may impact the uncertainty in determined ages (R Core Team, 2020). This approach is based on bootstrapping (random sampling with replacement 1000 times) to estimate the mean of three measures of variability, standard deviation, interquartile range (IQR), and range of the initial ratio. Additionally, the 95% confidence interval (CI) was constructed using random sampling with repetition for different sample size discussed in the results chapter. The codes applied in this approach is included in the Supplementary material.

This analysis was performed on groups of samples within specific clusters: (1) a complete set comprising 50 samples, (2) all 42 samples except samples from parasequence 6, based on its different provenance, (3) all 23 samples from parasequence 7, (4) 19 samples from proximal prodelta FA excluding parasequence 6 samples, and (5) all 14 samples from swamp FA.

4. Results

4.1. Authigenic $^{10}Be/^{9}Be$ ratio

Table 1 presents the values of measured natural $^{10}Be/^{9}Be$ ratio for 50 samples along with indication of their classification by FA and parasequence number. The distribution of obtained isotopic ratios along the well profiles is shown in Fig. 2 and their ascending distribution within parasequences and FA classes is depicted together with Kernel density estimation in Fig. 3. The overall measured authigenic $^{10}Be/^{9}Be$ ratio in these 50 samples (Fig. 2, Table 1) ranges from $1.27 \pm 0.03 \times 10^{-9}$ to $3.97 \pm 0.49 \times 10^{-9}$, the minimum value was obtained in sample EM 13–9.4 and maximum in EM 13–23.85, respectively. When considering the variability among samples from different parasequences, it is

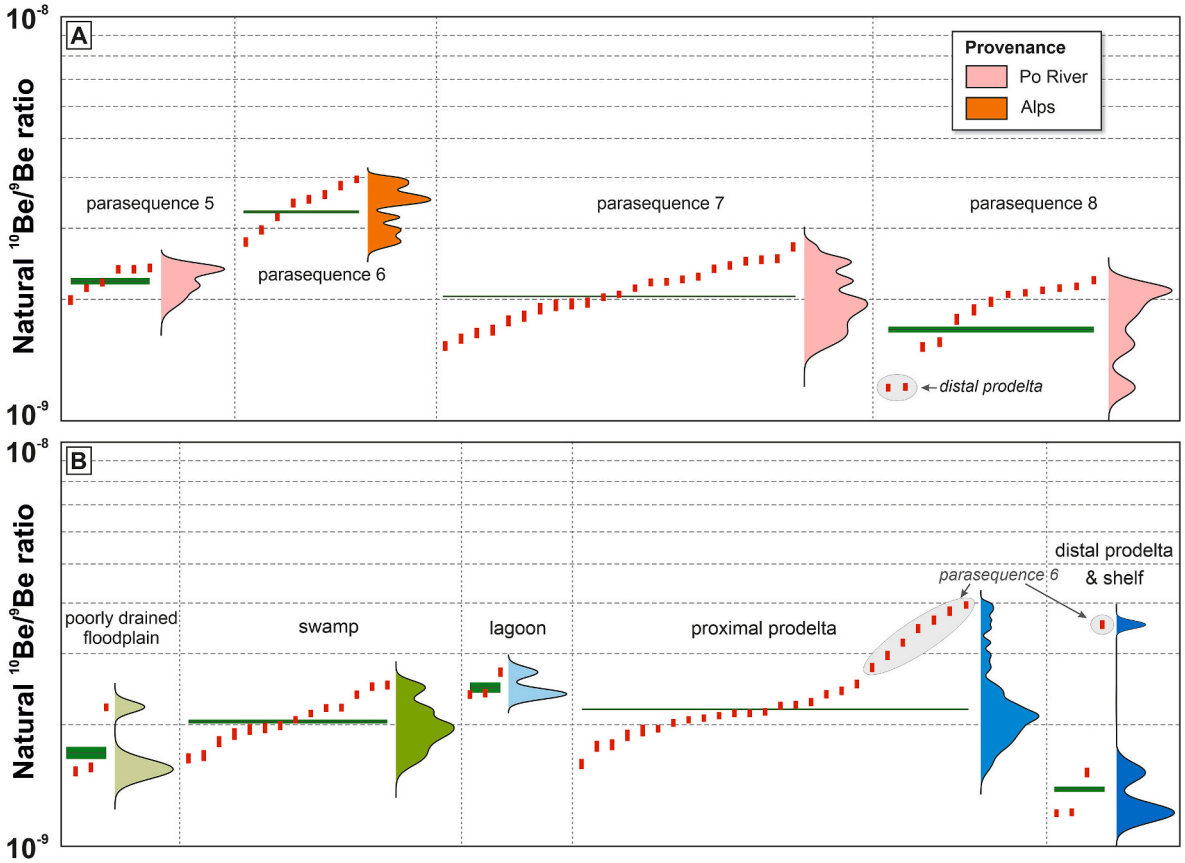

Fig. 3. (A) represents weighted mean (green line) of the ratio in different parasequences along with Kernel density estimation of the ratios obtained by the KDX software (Spencer et al., 2017). The weighted mean values of ratio (green line) as well as kernel density estimation for samples from different FA are visualized in (Fig. B). Note the logarithmic scale on the vertical axis with $^{10}Be/^{9}Be$ values. It is worth noting that the higher values for the ratios are observed in case of samples from parasequence 6 which deviates from the distribution of values of parasequences 5, 7 and 8. Noteworthy, the distribution of values is identical for swamp (topset) and proximal prodelta (foreset) facies associations (excluding samples of parasequence 6). Facies association and parasequence classification of samples based on Amorosi et al. (2017, 2019). (For interpretation of the references to colour in this figure legend, the reader is referred to the Web version of this article.)

observed that the samples from parasequence 6 exhibit significantly higher ratios than those from other parasequences (Fig. 3A). The ratio for two samples from EM 5 well has range of values increasing from 1.92 $\pm$ 0.04 $\times$ 10^{-9} to 2.56 $\pm$ 0.06 $\times$ 10^{-9}. EM 8 well yields the value of the isotopic ratio in the range 1.62 $\pm$ 0.04 $\times$ 10^{-9} to 2.44 $\pm$ 0.06 $\times$ 10^{-9}, and for EM 9 well the value of the ratio spans from 1.65 $\pm$ 0.04 10^{-9} to 2.54 $\pm$ 0.06 $\times$ 10^{-9}. EM 10 well yields isotopic ratios from 1.72 $\pm$ 0.04 10^{-9} to 2.74 $\pm$ 0.06 10^{-9} and in case of EM 13 well where maximum

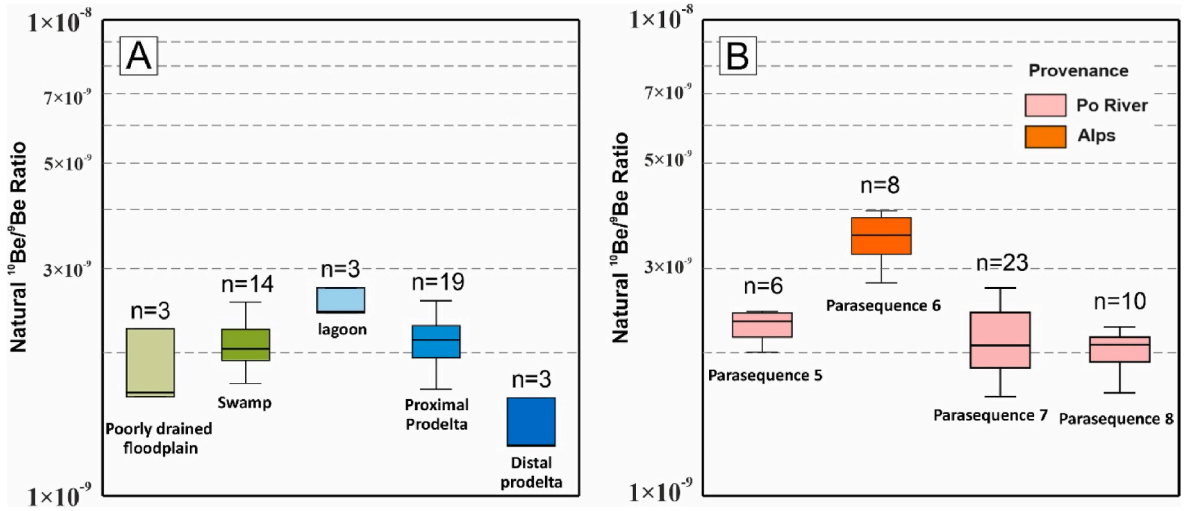

Fig. 4. Box plots (A) samples from different FA, in case of proximal prodelta FA, samples from parasequence 6 are excluded, (B) samples from different parasequences, in parasequence 8, the 3 samples from distal prodelta FA are excluded. Note the logarithmic scale on the vertical axis. Facies association and parasequence classification of samples based on Amorosi et al. (2017, 2019).

number of samples was taken the value scatters from 1.27 ± 0.03 10^{-9} to 3.97 ± 0.49 10^{-9}, if samples from parasequence 6 are included (Fig. 2).

Samples from parasequence 5 exhibit variability in the range from 2.01 ± 0.05 × 10^{-9} to 2.44 ± 0.06 × 10^{-9} (Table 1, Figs. 3 and 4). In case of parasequence 6 the distribution is much more widespread within and from other samples comparatively, the value ranges from 2.98 ± 0.07 × 10^{-9} to 3.97 ± 0.49 × 10^{-9}. The parasequence 7 samples show variability from 1.62 ± 0.04 × 10^{-9} to 2.74 ± 0.06 × 10^{-9} which is not much widespread if we consider that the parasequence 7 set consist of 25 samples. In case of parasequence 8 having a set of 13 samples the distribution ranges from 1.27 ± 0.03 × 10^{-9} to 2.27 ± 0.05 × 10^{-9}. However, if the samples from distal prodelta FA are exempted, the minimum ratio for these sets of samples increases to 1.65 ± 0.04 × 10^{-9}, making the distribution narrower (Fig. 3A).

Distinct $^{10}Be/^{9}Be$ values of parasequence 6 and 7 are evident in both the EM 13 log (Fig. 2A) and Kernel density estimations (Fig. 3A). The parasequences 5, 7 and 8 exhibit a very similar and relatively homogeneous distribution of values (Fig. 3A).

The variability within samples from different FAs has less widespread distribution (Fig. 3B). Three samples from poorly drained floodplain show variability in the range 1.62 ± 0.04 × 10^{-9} to 2.25 ± 0.05 × 10^{-9}. 14 samples from swamp FA yield ranges from 1.72 ± 0.04 × 10^{-9} to 2.56 ± 0.06 × 10^{-9}. Three samples from lagoonal FA exhibit the ratio between 2.42 ± 0.06 × 10^{-9} to 2.74 ± 0.06 × 10^{-9}. Samples from proximal prodelta have the ratio value in the range of 1.68 ± 0.04 × 10^{-9} to 2.57 ± 0.06 × 10^{-9}, in the case samples from parasequence 6 are excluded. However, adding the samples from parasequence 6 (Fig. 3B) widen the distribution and the highest ratio of 3.97 ± 0.49 × 10^{-9} is reached by the sample EM 13–23.85.

Another way to represent the variability in the natural $^{10}Be/^{9}Be$ ratio is depicted in Fig. 4 with the box plots (A) showing the variability of ratio in different facies. It should be noted that for the box plot of proximal prodelta FA, the samples from parasequence 6 are excluded. Thus, the median value and distribution of the ratio for swamp (14 samples) 2.03 × 10^{-9} and proximal prodelta FA (19 samples, except samples from parasequence 6) 2.12 × 10^{-9} representing the main volume of the samples appear as closer to each other. This can also be observed in Fig. 3B where KDE plots for samples from these two FAs shows peak at nearly identical values. The inclusion of samples from parasequence 6 in proximal prodelta facies will shift the median of ratio of this facies association group to higher values as compared to other facies associations. As it can be seen in Fig. 4B, not only the median of the ratio for samples from parasequence 6 lies significantly higher than the samples from the parasequences 5, 7 and 8, but the ranges barely overlap. The minimum ratio among all samples is observed in the three samples from distal prodelta FA belonging to parasequence 8. These three samples in the box plot Fig. 4B are excluded for the plot of parasequence 8, thus making of a very similar range with box plots of parasequence 5 and 7 samples.

The poorly drained floodplain, lagoon and distal prodelta FA sets have identical count of 3 samples, though the median of samples from these three FAs differs significantly, reaching 1.64 × 10^{-9}, 2.03 × 10^{-9}, and 1.27 × 10^{-9} respectively.

4.2. Elemental concentrations in authigenic phase

The analyzed samples yielded concentrations of authigenic iron in the range of 38.4–158.0 ppm (Supplementary Table S2), with a relatively scattered distribution when plotted against the authigenic $^{10}Be/^{9}Be$ (Fig. 5A). The scattered pattern is valid especially for the delta plain FA (poorly drained floodplain and swamp). A closer look on the proximal prodelta FA allows to observe a weak correlation with R^2 = 0.256 (*sensu* Walpole et al., 2012) (Fig. 5B). A similarly dispersed pattern could be observed also in the case of the authigenic manganese, reaching values of 0.43–13.87 ppm (Fig. 5C). Notably, the poorly

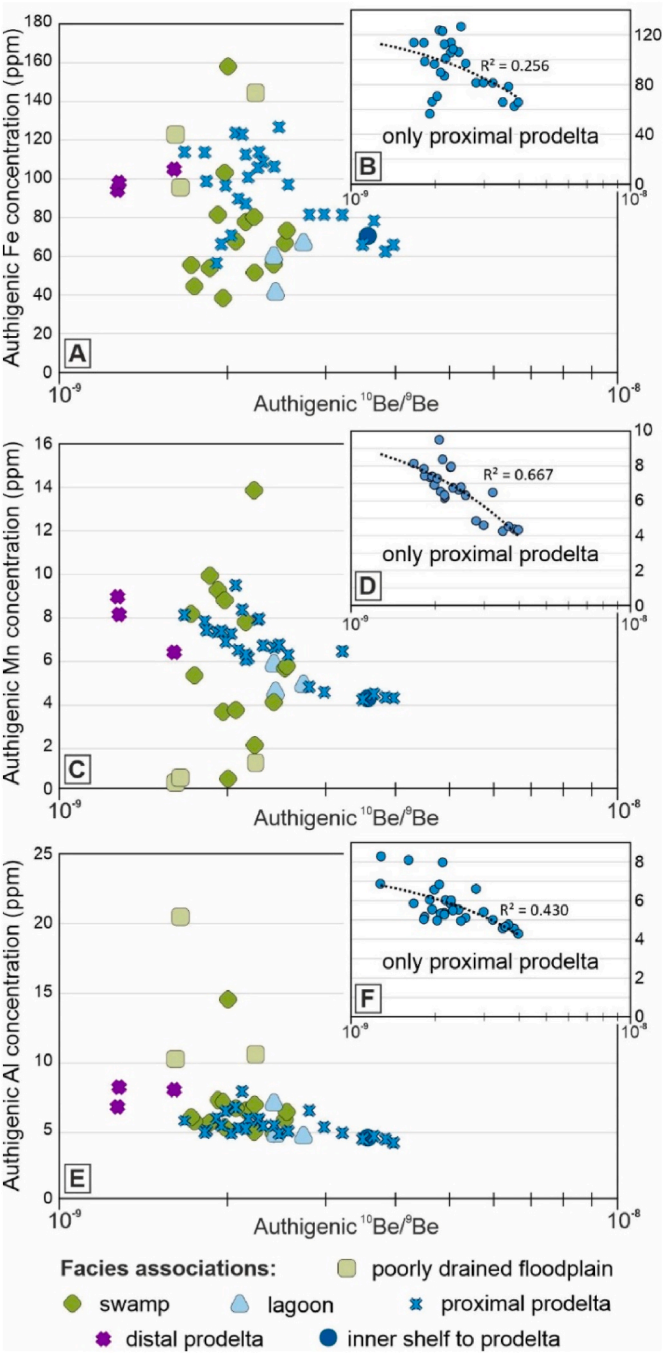

Fig. 5. Elemental concentrations of Fe (A, B), Mn (C, D) and Al (E, F) in the authigenic phase of the studied samples, plotted against the natural authigenic $^{10}Be/^{9}Be$. Facies association classification of samples based on Amorosi et al. (2017, 2019). Most of FA exhibit scattered distribution, except for the proximal prodelta samples shown in the inset graphs. Note the logarithmic scale on the horizontal axis with $^{10}Be/^{9}Be$ values.

drained floodplain samples represent the lowermost concentration extreme. Again, the juxtaposition of the proximal prodelta samples with authigenic $^{10}Be/^{9}Be$ gives a different picture with a moderately strong correlation reaching R^2 = 0.667 (*sensu* Walpole et al., 2012) (Fig. 5D).

The samples show a less scattered distribution in the case of authigenic aluminum plotted alongside the authigenic $^{10}Be/^{9}Be$, with highest frequency in the range of ~4–8 ppm (Fig. 5E). When focusing only on the prodelta samples, a moderate correlation with R^2 = 0.430 could be observed (*sensu* Walpole et al., 2012) (Fig. 5E). Distal prodelta samples appear as extreme values on the correlation trend of the proximal

prodelta set, having the lowest authigenic $^{10}Be/^{9}Be$ and highest Mn and Al concentrations (Fig. 5C–E).

The lowest concentration of Be and Al (Supplementary Table S2) in the authigenic phase observed in the samples from parasequence 6 also supports the statement that these samples have different provenance than samples from the latter parasequences.

4.3. Sample size dependency of the variability in $^{10}Be/^{9}Be$ ratio

To assess the dependency of variability in the initial $^{10}Be/^{9}Be$ ratio on the number of samples, as observed in Holocene Po plain and thus to estimate the variability in initial ratio that is unrelated to age differences (i.e., as the half-life of the cosmogenic ^{10}Be is 1.387 ± 0.01 Ma, Holocene Po plain samples effectively capture the initial $^{10}Be/^{9}Be$), we have resampled the empirical distribution of the initial $^{10}Be/^{9}Be$ 1000 times and estimated the mean range, IQR and standard deviation in the initial $^{10}Be/^{9}Be$ (and 95% confidence intervals) as the sample size increases from 2 to 50 (Fig. 6). As the empirical values of ratio obtained in our study are not necessarily normally distributed, random sampling with replacement (bootstrapping) seems to be a suitable option to evaluate the sample size dependency of the variability in initial ratio and to assess the resulting effect on the minimum estimate of age error. We used three measures of variability, including standard deviation (SD), inter-quartile range (IQR), and total range. The first two measures are less sensitive to outliers (assuming that distributions are not strongly skewed or heavy-tailed) than the total range. Supplementary Fig. S2 illustrates this approach for rest of the data clusters (2–5) mentioned in Section 3.4. This approach shows that both standard deviation and inter-quartile range in the initial $^{10}Be/^{9}Be$ stabilize as the number of samples exceeds ~10. Furthermore, the range in the initial $^{10}Be/^{9}Be$ is most sensitive to outliers, underscoring the importance of averaging across multiple samples rather than relying on isolated ones for age estimates.

Any non-zero variability in the initial $^{10}Be/^{9}Be$ naturally directly propagates into age uncertainty. The magnitude of this effect as a function of sample size was approximated by assessing the variability in age conditional on the initial ratio (i.e., age is equal to 1/decay constant × log (initial ratio/true ratio)), with the mean of the initial ratio taken as the true ratio. This variability was estimated under increasing sample size with the same bootstrapping procedure as specified above. The variability in the initial ratio (as observed in the Holocene of the Po coastal plain) can be expected to propagate into the standard deviation or IQR in age uncertainty that attains 0.5–1.0 Myr. In this case, once the number of samples exceeds 10–20, the variability in the initial ratio and in age variability remains stable. The age range leads to errors that can attain 2 Myr as each sample contributes to the total age range estimate (bottom row in Fig. 6).

Fig. 6 shows that the sample size exceeding ~10 has better ability to capture the variation in the initial $^{10}Be/^{9}Be$ when geochronological ages of sampling units (members or formations) are based on multiple samples, rather than on isolated samples. As the sample size increases, it becomes more likely that variability in the initial $^{10}Be/^{9}Be$ will be representative of the original variability. The same statistical approach applied to the set of 42 samples after the exclusion of the samples from parasequence 6 suggests that sample size exceeding ~7 to 15 will capture the variability in the initial $^{10}Be/^{9}Be$ ratio (Supplementary Fig. S2). Hence, exclusion of samples from parasequence 6 with different provenance makes the distribution of ratio less variable, with necessity of less samples to capture its narrower natural $^{10}Be/^{9}Be$ range. Similarly, the cluster of samples from parasequence 7, samples from proximal predelta FA (without parasequence 6 samples), and samples from swamp FA yields a necessary sample count of more than ~5–7, ~5–7, and ~4–6, respectively to capture the variability and corresponding estimate of age error based on standard deviation statistics of the initial ratio. Nevertheless, an effect of autocorrelation may potentially bias the estimate for clusters 3–5 (Supplementary Fig. S2), as the initial sample count is significantly lower.

As swamp (n = 14) and proximal prodelta (n = 19, except samples from parasequence 6) sample sets analyzed in this study have the greatest number of samples, their mean absolute deviation might be suggested to predict the uncertainty arising due to variation in the ratio. For instance, the mean absolute deviation of the ratio for sample set of swamp facies deviates from the mean by ~10%. Similarly, for proximal prodelta samples, the mean absolute deviation appears to be ~8% and for the complete group of 33 samples consisting of swamp and proximal prodelta FA samples shows a deviation from the grouped mean of these two FA value by ~9%.

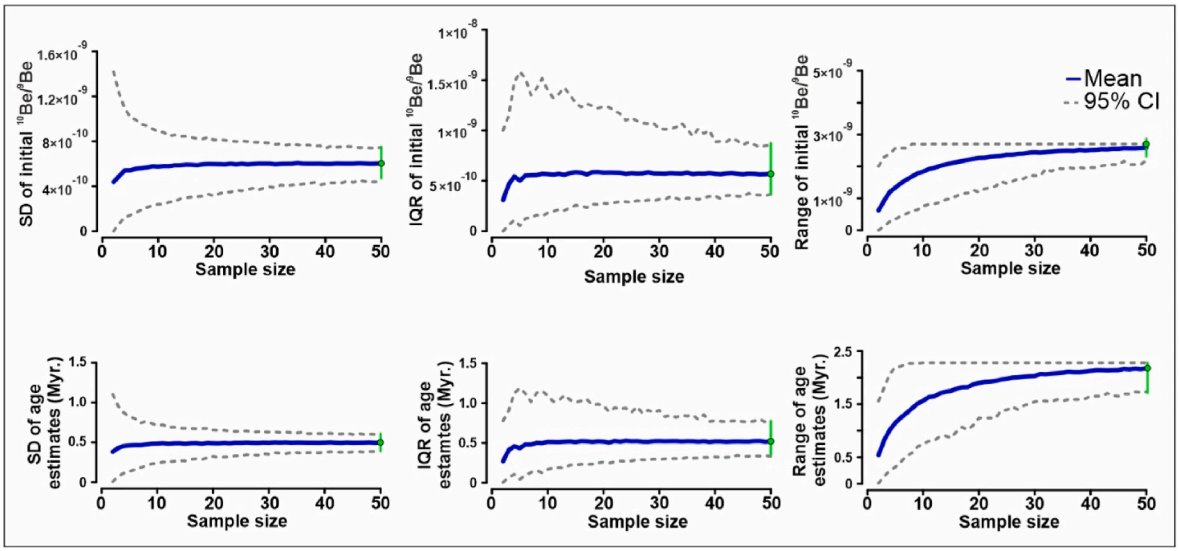

Fig. 6. Sample-size dependency of the initial $^{10}Be/^{9}Be$ ratio and of the corresponding age error related purely to that variability. Variability in the initial $^{10}Be/^{9}Be$ ratio is estimated from bootstrapping repeated 1000 times. The solid blue lines correspond to the mean variability and the dashed gray to the 95% confidence intervals. As raw bootstrapped estimates of variability are slightly biased down, the green circle and the green lines at n = 50 represents the mean and lower and upper 95% confidence bounds that correct for the bias (Krause et al., 2010). The X-axis shows the number of samples. (The dataset in this Fig. consists of complete 50 samples, for rest of the clusters 2–5 mentioned in Section 3.4, please refer to Supplementary Fig. S2). (For interpretation of the references to colour in this figure legend, the reader is referred to the Web version of this article.)

5. Discussion – effects driving the authigenic $^{10}Be/^{9}Be$

5.1. Hypothesis 1 – effect of provenance switch on the authigenic $^{10}Be/^{9}Be$ ratio

The samples from parasequences 6 exhibit significantly higher $^{10}Be/^{9}Be$ ratio compared to samples from parasequences 5, 7 and, 8. The parasequences 6 has provenance traced back to Alpine rivers while rest of the parasequences were deposited by the Po River, as indicated for example by chromium elemental concentrations as a tracer of volcanic rocks (Amorosi et al., 2020). Thus, the obtained results confirm Hypothesis 1, suggesting that the change in provenance plays a role in the variation of the authigenic $^{10}Be/^{9}Be$ ratio.

Such variation needs to be taken into consideration while applying this dating method to alluvial, deltaic and even deep water sediments deposited by gravity flows. Switching of provenance with contrasting petrological properties is particularly likely in active orogens and basin systems actively subsiding in late Cenozoic (Horton and Schmitt, 1998; Kováč et al., 2018; Breitfeld et al., 2023). Failure to recognize the effect of provenance in the studied depositional record could lead to an offset in the calculated age of approximately 1 Myr (considering the weighted mean ratios of parasequences 6 and 7). Such change might be also incorrectly interpreted as a temporal change in denudation rates (e.g., von Blanckenburg et al., 2012; von Blanckenburg and Bouchez, 2014; Rahaman et al., 2017; Dannhaus et al., 2018; Portenga et al., 2019) and thus the observed variation in $^{10}Be/^{9}Be$ ratio highlights the importance of caution in provenance analysis in beryllium isotope studies.

5.2. Hypothesis 2 – effect of sedimentary environment change on the authigenic $^{10}Be/^{9}Be$ ratio

The swamp and proximal prodelta samples constitute the majority of the dataset (Figs. 3 and 4), making it reasonable to compare these two sets of samples as representatives of delta topset dominated by riverine $^{10}Be/^{9}Be$ signature and of delta foreset passing towards the open sea. Samples from parasequences 6 were excluded from the set of proximal prodelta samples, as they were proven to deviate due to the provenance variation. Despite the prodelta facies being deposited in basinal environment where the formation of an outer rim from basinal waters might be expected (Wittmann et al., 2017; Kong et al., 2021), such signal from basinal waters is not observed in our study. The authigenic $^{10}Be/^{9}Be$ ratios for swamp samples are statistically identical to those of the samples from proximal prodelta. An explanation of this similarity could be found in the prevalence of hyperpycnal flow depositional processes on the proximal prodelta, since the sampled succession is deposited by a river-dominated deltaic system (Amorosi et al., 2019; Pellegrini et al., 2021, 2023). Hence, the initial $^{10}Be/^{9}Be$ ratio is expected to maintain the riverine signature even on the prodelta slope, leading to the rejection of Hypothesis 2.

The prodelta depositional processes were rapid and high accumulation rates reaching the order of ~100 mm × a^{-1} in the EM 13 well allowed for burial without significant overwriting the riverine signature by a post-depositional growth of outer authigenic rim from basinal waters. However, a moderately strong correlation of the authigenic $^{10}Be/^{9}Be$ with authigenic Mn concentration (Fig. 5D) provides a clue for the variability within the proximal prodelta FA. Based on the recent observations by Deng et al. (2023), this correlation hints to the possible enrichment by ^{9}Be released diagenetically from pore waters. This might be even supported by the low $^{10}Be/^{9}Be$ values of the three distal prodelta samples, which may represent an end member with the highest influence of the described effect. Temporal stochastic variations in accumulation rate and strata burial likely drive the pace of ^{9}Be pore water release, influencing the authigenic $^{10}Be/^{9}Be$ variability within prodelta FA.

Contrary to this observation, another well-represented swamp FA exhibit scattered distribution of elemental concentrations plotted towards authigenic $^{10}Be/^{9}Be$ (Fig. 5), implying absence of penecontemporary or post-depositional process governing modification of beryllium isotopic signature in depositional record. As the delta plain environment and especially swamp is not prone to extensive pedogenic processes due to high ground-water level and its poorly drained nature (Campo et al., 2016, 2017), the observed authigenic $^{10}Be/^{9}Be$ variation within swamp FA is more likely the result of changes in beryllium isotopic fluxes before deposition rather than modification during early burial.

Despite the high scatter of the poorly drained floodplain samples, the two lowest authigenic $^{10}Be/^{9}Be$ values might result from a relatively increased pedogenesis in comparison to the remaining delta plain FA, which would be supported by the highest Al and Fe concentration in the authigenic phase. However, the increased exposure to pedogenesis is expected to result in the case of the present-day MAP of 650 mm (Brunetti et al., 2000) in a relative ^{10}Be enrichment (e.g, Dixon et al., 2018). More samples taken from the floodplain environment in future research may help to resolve this contra-intuitive observation.

It is worth mentioning that the sample set excluding parasequence 6 and distal prodelta samples (being extremes likely due to the lower depositional rates) reach minimum and maximum authigenic $^{10}Be/^{9}Be$ ratios of 2.74×10^{-9} and 1.62×10^{-9}, respectively. Their difference equals to a^{10}Be decay duration of 1.056 Myr. However, we consider using such a wide uncertainty as overestimation even for smaller sample sets, as it is based on limiting values.

6. Summary and conclusions

The primary challenge in authigenic $^{10}Be/^{9}Be$ dating method lies in accurately determining the initial ratio. Overestimating the mean initial ratio can lead to an apparently older calculated age of the sediment comparing to the actual value. Therefore, understanding the variability of beryllium isotopic fluxes, their preservation in the depositional record and their predictability is essential for developing representative geochronological models.

The current applications of the authigenic $^{10}Be/^{9}Be$ dating yield age uncertainties associated with the analytical uncertainties in determination of the isotopic concentrations of the dated samples, uncertainty of the ^{10}Be half-life, and the variability of the authigenic $^{10}Be/^{9}Be$ values from the samples used to establish the initial $^{10}Be/^{9}Be$ ratio. However, the application of dating may also require consideration of the uncertainties stemming from the environmental variability of the beryllium isotopic signature and its preservation in a depositional record. This factor, related to stochastic variations such as oscillation of sediment delivery, accumulation rate and strata burial, should be considered, especially in cases where there is a lower number of samples taken for dating. Conversely, a sufficiently high number of dating samples should statistically represent the environmental variability, and determining such a threshold in sample count was the objective here.

One of the important prerequisites in $^{10}Be/^{9}Be$ dating method is that the samples chosen for initial ratio determination should be from a "recent" (<200 ka) sediment deposited in similar FA as sample of interest to be dated was deposited (e.g., Lebatard et al., 2010). It is therefore important to have a consistent value of authigenic $^{10}Be/^{9}Be$ ratio for the samples chosen from a particular type of FA. Failure to obtain a reliable initial ratio can result in incorrect ages, for example in Jeong et al. (2023), incorrect estimation of the initial ratio resulted in significantly younger age of the sediment in comparison to independent proxies.

Nevertheless, the low variability in authigenic $^{10}Be/^{9}Be$ observed in this study implies that any FA of a highstand deltaic succession could be dated using the initial ratio obtained from any of the highstand delta plain and prodelta facies, except for the distal prodelta to shelf FA characteristic by low sediment supply. Sampling the most closely related FA both for dating and initial ratio is the safest approach regardless. When selecting a site for initial ratio, it is crucial to look for similar pace of sedimentation and burial as the succession to be dated.

On the other hand, the variation in ratio arising due to switch in the provenance, can also affect the sample count necessary for initial ratio determination. As observed from random sampling and bootstrapping, excluding all samples from Parasequences 6 reduced the minimum sample size needed to capture the variability from ~10 to ~7. This implies that with the effective knowledge of provenance, the variability in the ratio can be narrowed down, leading to a more efficient and accurate determination of the final initial ratio.

To suggest the best suitable statistics in order to depict the ratio variability in this study (from the Holocene of the Po coastal plain), we provided an insight into the three different statistics used. Range might be affected in some cases by extreme outlier arising due post depositional processes altering the ratio, and IQR may cover the 50% of the variability. However, SD might be suggested as the most reliable statistics as it depicts the variation around the mean ratio observed in the dataset.

The highstand deltaic system, as observed in the normal regressive Holocene deposits of the Po Plain, appears as relatively homogeneous in terms of the authigenic $^{10}Be/^{9}Be$ isotopic signature in its depositional record. The statistical analysis indicates that $n > 10$ samples may fully cover the paleoenvironmental variability of the system for dating. In the case of lower number of samples, an additional uncertainty of 9% shall quantify the paleoenvironmental variability for individual ages, as defined by the mean absolute deviation of the swamp and proximal prodelta sample sets. To expand the utility of authigenic $^{10}Be/^{9}Be$ in geochronology, further studies are necessary to investigate its variability across different depositional systems, such as tide-dominated deltas or offshore environments influenced by the interplay of riverine and contour currents.

CRediT authorship contribution statement

Kishan Aherwar: Writing – review & editing, Writing – original draft, Visualization, Software, Methodology, Investigation, Formal analysis, Data curation, Conceptualization. **Michal Šujan:** Writing – review & editing, Writing – original draft, Visualization, Validation, Supervision, Software, Resources, Project administration, Methodology, Investigation, Funding acquisition, Formal analysis, Data curation, Conceptualization. **Alessandro Amorosi:** Validation, Supervision, Methodology, Formal analysis, Data curation, Conceptualization. **Bruno Campo:** Writing – review & editing, Writing – original draft, Validation, Investigation, Formal analysis, Data curation, Conceptualization. **Andrej Chyba:** Writing – original draft, Validation, Methodology, Formal analysis, Data curation. **Adam Tomašových:** Writing – review & editing, Writing – original draft, Visualization, Software, Methodology, Data curation, Conceptualization. **Barbara Rózsová:** Methodology, Investigation, Data curation. **Aster Team:** Software, Methodology, Data curation. **Régis Braucher:** Writing – review & editing, Validation, Supervision, Software, Methodology, Data curation, Conceptualization.

Declaration of competing interest

The authors declare that they have no known competing financial interests or personal relationships that could have appeared to influence the work reported in this paper.

Data availability

Data will be made available on request.

Acknowledgements

The study was supported by the Slovak Research and Development Agency (APVV) under contracts Nos. APVV-16-0121, APVV-20-0120 and APVV-21-0281, and by the Scientific Grant Agency of the Ministry of Education, Science, Research and Sport of the Slovak Republic and the Slovak Academy of Sciences (VEGA) under the contract No. 1/0346/20. ASTER AMS, national facility (CEREGE, Aix en Provence), is supported by the INSU/CNRS and IRD and member of AIX MARSEILLE PLATFORMS and REGEF networks. Anonymous reviewer is thanked for the constructive comments, which helped to improve the clarity of the manuscript.

Appendix A. Supplementary data

Supplementary data to this article can be found online at https://doi.org/10.1016/j.qsa.2024.100201.

References

Amorosi, A., Barbieri, G., Bruno, L., Campo, B., Drexler, T.M., Hong, W., Rossi, V., Sammartino, I., Scarponi, D., Vaiani, S.C., 2019. Three-fold nature of coastal progradation during the Holocene eustatic highstand, Po Plain, Italy–close correspondence of stratal character with distribution patterns. Sedimentology 66, 3029–3052.

Amorosi, A., Bruno, L., Campo, B., Costagli, B., Dinelli, E., Hong, W., Sammartino, I., Vaiani, S.C., 2020. Tracing clinothem geometry and sediment pathways in the prograding Holocene Po Delta system through integrated core stratigraphy. Basin Res. 32, 206–215.

Amorosi, A., Bruno, L., Campo, B., Morelli, A., Rossi, V., Scarponi, D., Hong, W., Bohacs, K.M., Drexler, T.M., 2017. Global sea-level control on local parasequence architecture from the Holocene record of the Po Plain. Italy. Marine and Petroleum Geology 87, 99–111.

Aslan, A., Autin, W.J., 1999. Evolution of the Holocene Mississippi River floodplain, Ferriday, Louisiana; insights on the origin of fine-grained floodplains. J. Sediment. Res. 69, 800–815.

Bacon, A.R., Richter, D.d., Bierman, P.R., Rood, D.H., 2012. Coupling meteoric ^{10}Be with pedogenic losses of ^{9}Be to improve soil residence time estimates on an ancient North American interfluve. Geology 40, 847–850.

Barg, E., Lal, D., Pavich, M., Caffee, M., Southon, J., 1997. Beryllium geochemistry in soils: evaluation of $^{10}Be/^{9}Be$ ratios in authigenic minerals as a basis for age models. Chem. Geol. 140, 237–258.

Boccaletti, M., Corti, G., Martelli, L., 2011. Recent and active tectonics of the external zone of the Northern Apennines (Italy). Int. J. Earth Sci. 100, 1331–1348.

Botka, D., Magyar, I., Csoma, V., Tóth, E., Šujan, M., Ruszkiczay-Rüdiger, Z., Chyba, A., Braucher, R., Sant, K., Ćorić, S., 2019. Integrated stratigraphy of the Guşteriţa clay pit: a key section for the early Pannonian (late Miocene) of the Transylvanian Basin (Romania). Austrian Journal of Earth Sciences 112, 221–247.

Bourlès, D., Raisbeck, G., Yiou, F., 1989. ^{10}Be and ^{9}Be in marine sediments and their potential for dating. Geochem. Cosmochim. Acta 53, 443–452.

Braucher, R., Guillou, V., Bourlès, D.L., Arnold, M., Aumaître, G., Keddadouche, K., Nottoli, E., 2015. Preparation of ASTER in-house $^{10}Be/^{9}Be$ standard solutions. Nucl. Instrum. Methods Phys. Res. Sect. B Beam Interact. Mater. Atoms 361, 335–340.

Breitfeld, H.T., Hennig-Breitfeld, J., Anthony, G., BouDagher-Fadel, M., Vermeesch, P., Lünsdorf, K., Rösel, D., Konrad-Schmolke, M., Gilbricht, S., 2023. The onshore west Baram delta deposits: provenance and drainage in the middle Miocene to pliocene in NW borneo and comparison to the champion delta. Mar. Petrol. Geol. 158, 106537.

Brown, E.T., Measures, C.I., Edmond, J.M., Bourlès, D.L., Raisbeck, G.M., Yiou, F., 1992. Continental inputs of beryllium to the oceans. Earth Planet Sci. Lett. 114, 101–111.

Brunetti, M., Buffoni, L., Maugeri, M., Nanni, T., 2000. Precipitation intensity trends in northern Italy. Int. J. Climatol.: A Journal of the Royal Meteorological Society 20, 1017–1031.

Bruno, L., Bohacs, K.M., Campo, B., Drexler, T.M., Rossi, V., Sammartino, I., Scarponi, D., Hong, W., Amorosi, A., 2017. Early Holocene transgressive palaeogeography in the Po coastal plain (northern Italy). Sedimentology 64, 1792–1816.

Burrato, P., Ciucci, F., Valensise, G., 2003. An inventory of river anomalies in the Po Plain, Northern Italy: evidence for active blind thrust faulting. Ann. Geophys.46. https://doi.org/10.4401/ag-3459.

Campo, B., Amorosi, A., Bruno, L., 2016. Contrasting alluvial architecture of Late Pleistocene and Holocene deposits along a 120-km transect from the central Po Plain (northern Italy). Sediment. Geol. 341, 265–275.

Campo, B., Amorosi, A., Vaiani, S.C., 2017. Sequence stratigraphy and late Quaternary paleoenvironmental evolution of the Northern Adriatic coastal plain (Italy). Palaeogeogr. Palaeoclimatol. Palaeoecol. 466, 265–278.

Carcaillet, J., Bourlès, D.L., Thouveny, N., Arnold, M., 2004. A high resolution authigenic $^{10}Be/^{9}Be$ record of geomagnetic moment variations over the last 300 ka from sedimentary cores of the Portuguese margin. Earth Planet Sci. Lett. 219, 397–412.

Carminati, E., Doglioni, C., 2012. Alps vs. Apennines: the paradigm of a tectonically asymmetric Earth. Earth Sci. Rev. 112, 67–96.

Cattaneo, A., Correggiari, A., Langone, L., Trincardi, F., 2003. The late-Holocene Gargano subaqueous delta, Adriatic shelf: sediment pathways and supply fluctuations. Mar. Geol. 193, 61–91.

Cattaneo, A., Trincardi, F., Asioli, A., Correggiari, A., 2007. The Western Adriatic shelf clinoform: energy-limited bottomset. Continent. Shelf Res. 27, 506–525.

Chmeleff, J., von Blanckenburg, F., Kossert, K., Jakob, D., 2010. Determination of the ^{10}Be half-life by multicollector ICP-MS and liquid scintillation counting. Nucl. Instrum. Methods Phys. Res. Sect. B Beam Interact. Mater. Atoms 268, 192–199.

Correggiari, A., Cattaneo, A., Trincardi, F., 2005. The modern Po Delta system: lobe switching and asymmetric prodelta growth. Mar. Geol. 222, 49–74.
Dannhaus, N., Wittmann, H., Krám, P., Christl, M., von Blanckenburg, F., 2018. Catchment-wide weathering and erosion rates of mafic, ultramafic, and granitic rock from cosmogenic meteoric $^{10}Be/^{9}Be$ ratios. Geochem. Cosmochim. Acta 222, 618–641.
Deng, K., Rickli, J., Suhrhoff, T.J., Du, J., Scholz, F., Severmann, S., Yang, S., McManus, J., Vance, D., 2023. Dominance of benthic fluxes in the oceanic beryllium budget and implications for paleo-denudation records. Sci. Adv. 9, eadg3702.
Dixon, J.L., Chadwick, O.A., Pavich, M.J., 2018. Climatically controlled delivery and retention of meteoric ^{10}Be in soils. Geology 46, 899–902.
Graham, I.J., Ditchburn, R.G., Whitehead, N.E., 1998. ^{10}Be spikes in Plio–Pleistocene cyclothems, Wanganui Basin, New Zealand: identification of the local flooding surface (LFS). Sediment. Geol. 122, 193–215.
Graly, J.A., Bierman, P.R., Reusser, L.J., Pavich, M.J., 2010. Meteoric ^{10}Be in soil profiles–a global meta-analysis. Geochem. Cosmochim. Acta 74, 6814–6829.
Greggio, N., Giambastiani, B.M., Balugani, E., Amaini, C., Antonellini, M., 2018. High-resolution electrical resistivity tomography (ERT) to characterize the spatial extension of freshwater lenses in a salinized coastal aquifer. Water 10, 1067.
Horton, B.K., Schmitt, J.G., 1998. Development and exhumation of a Neogene sedimentary basin during extension, east-central Nevada. Geol. Soc. Am. Bull. 110, 163–172.
Jeong, A., Seong, Y.B., Gootee, B.F., Yu, B.Y., Cheung, S.Y., 2023. Application and limitations of the authigenic $^{10}Be/^{9}Be$ dating and meteoric ^{10}Be inventory in Bouse Formation along the lower Colorado River corridor, southwestern USA. Episodes Journal of International Geoscience 46, 85–97.
Kong, W., Zhou, L., AsterTeam, 2021. Tracing water masses and assessing boundary scavenging intensity with beryllium isotopes in the northern south China sea. J. Geophys. Res.: Oceans 126, e2021JC017236.
Korschinek, G., Bergmaier, A., Faestermann, T., Gerstmann, U., Knie, K., Rugel, G., Wallner, A., Dillmann, I., Dollinger, G., Von Gostomski, C.L., 2010. A new value for the half-life of ^{10}Be by heavy-ion elastic recoil detection and liquid scintillation counting. Nucl. Instrum. Methods Phys. Res. Sect. B Beam Interact. Mater. Atoms 268, 187–191.
Kováč, M., Rybár, S., Halásová, E., Hudáčková, N., Šarinová, K., Šujan, M., Baranyi, V., Kováčová, M., Ruman, A., Kľučiar, T., 2018. Changes in Cenozoic depositional environment and sediment provenance in the Danube Basin. Basin Res. 30, 97–131.
Krause, R.A., Barbour, S.L., Kowalewski, M., Kaufman, D.S., Romanek, C.S., Simoes, M. G., Wehmiller, J.F., 2010. Quantitative comparisons and models of time-averaging in bivalve and brachiopod shell accumulations. Paleobiology 36, 428–452.
Lebatard, A.-E., Bourlès, D.L., Braucher, R., Arnold, M., Duringer, P., Jolivet, M., Moussa, A., Deschamps, P., Roquin, C., Carcaillet, J., 2010. Application of the authigenic $^{10}Be/^{9}Be$ dating method to continental sediments: reconstruction of the Mio-Pleistocene sedimentary sequence in the early hominid fossiliferous areas of the northern Chad Basin. Earth Planet Sci. Lett. 297, 57–70.
Lebatard, A.-E., Bourlès, D.L., Duringer, P., Jolivet, M., Braucher, R., Carcaillet, J., Schuster, M., Arnaud, N., Monié, P., Lihoreau, F., 2008. Cosmogenic nuclide dating of Sahelanthropus tchadensis and Australopithecus bahrelghazali: mio-Pliocene hominids from Chad. Proc. Natl. Acad. Sci. USA 105, 3226–3231.
Lin, P., Song, Y., Zhan, W., Tian, R., Wang, Z., Xu, X., Luo, L., Abbas, M., Lai, Z., 2023. Late Pleistocene to Holocene sedimentary history in the pearl River Delta revealed by OSL and radiocarbon dating. Catena 224, 106972.
Lisé-Pronovost, A., Fletcher, M.-S., Simon, Q., Jacobs, Z., Gadd, P.S., Heslop, D., Herries, A.I., Yokoyama, Y., team, A., 2021. Chronostratigraphy of a 270-ka sediment record from Lake Selina, Tasmania: combining radiometric, geomagnetic and climatic dating. Quat. Geochronol. 62, 101152.
Magyar, I., Sztanó, O., Sebe, K., Katona, L., Csoma, V., Görög, Á., Tóth, E., Szuromi-Korecz, A., Šujan, M., Braucher, R., 2019. Towards a high-resolution chronostratigraphy and geochronology for the pannonian stage: significance of the paks cores (central pannonian basin). Foldtani Kozlony 149, 351.
Measures, C., Edmond, J., 1983. The geochemical cycle of ^{9}Be: a reconnaissance. Earth Planet Sci. Lett. 66, 101–110.
Merchel, S., Beutner, S., Opel, T., Rugel, G., Scharf, A., Tiessen, C., Weiß, S., Wetterich, S., 2019. Attempts to understand potential deficiencies in chemical procedures for AMS. Nucl. Instrum. Methods Phys. Res. Sect. B Beam Interact. Mater. Atoms 456, 186–192.
Merchel, S., Herpers, U., 1999. An update on radiochemical separation techniques for the determination of long-lived radionuclides via accelerator mass spectrometry. Radiochim. Acta 84, 215–220.
McHargue, L., Jull, A., Cohen, A., 2011. Measurement of ^{10}Be from Lake Malawi (Africa) drill core sediments and implications for geochronology. Palaeogeogr. Palaeoclimatol. Palaeoecol. 303, 110–119.
Middelburg, J.J., Soetaert, K., Herman, P.M., 1997. Empirical relationships for use in global diagenetic models. Deep Sea Res. Oceanogr. Res. Pap. 44, 327–344.
Nienhuis, J.H., Kim, W., Milne, G.A., Quock, M., Slangen, A.B.A., Törnqvist, T.E., 2023. River deltas and seasea-level rise. Annu. Rev. Earth Planet Sci. 51, 79–104.
Ori, G.G., 1993. Continental depositional systems of the Quaternary of the Po Plain (northern Italy). Sediment. Geol. 83, 1–14.
Patruno, S., Helland-Hansen, W., 2018. Clinoforms and clinoform systems: review and dynamic classification scheme for shorelines, subaqueous deltas, shelf edges and continental margins. Earth Sci. Rev. 185, 202–233.
Pellegrini, C., Patruno, S., Helland-Hansen, W., Steel, R.J., Trincardi, F., 2020. Clinoforms and clinothems: fundamental elements of basin infill. Basin Res. 32, 187–205.
Pellegrini, C., Sammartino, I., Schieber, J., Tesi, T., Paladini de Mendoza, F., Rossi, V., Chiggiato, J., Schroeder, K., Gallerani, A., Langone, L., 2023. On depositional processes governing along-strike facies variations of fine-grained deposits: unlocking the Little Ice Age subaqueous clinothems on the Adriatic shelf. Sedimentology71 941–973.
Pellegrini, C., Tesi, T., Schieber, J., Bohacs, K.M., Rovere, M., Asioli, A., Nogarotto, A., Trincardi, F., 2021. Fate of terrigenous organic carbon in muddy clinothems on continental shelves revealed by stratal geometries: insight from the Adriatic sedimentary archive. Global Planet. Change 203, 103539.
Picotti, V., Pazzaglia, F.J., 2008. A new active tectonic model for the construction of the Northern Apennines mountain front near Bologna (Italy). J. Geophys. Res. Solid Earth 113.
Pieri, M., Groppi, G., 1981. Subsurface Geological Structure of the Po Plain. Verlag nicht ermittelbar, Italy.
Portenga, E.W., Bierman, P.R., Trodick, C.D., Greene, S.E., DeJong, B.D., Rood, D.H., Pavich, M.J., 2019. Erosion rates and sediment flux within the Potomac River basin quantified over millennial timescales using beryllium isotopes. GSA Bulletin 131, 1295–1311.
Rahaman, W., Wittmann, H., von Blanckenburg, F., 2017. Denudation rates and the degree of chemical weathering in the Ganga River basin from ratios of meteoric cosmogenic ^{10}Be to stable ^{9}Be. Earth Planet Sci. Lett. 469, 156–169.
Raisbeck, G., Yiou, F., Fruneau, M., Loiseaux, J., Lieuvin, M., Ravel, J., 1981. Cosmogenic $^{10}Be/^{7}Be$ as a probe of atmospheric transport processes. Geophys. Res. Lett. 8, 1015–1018.
R Core Team, 2020. R: A Language and Environment for Statistical Computing. R Foundation for Statistical Computing, Vienna, Austria. Available online: http://www.r-project.org/index.html. (Accessed 12 May 2021).
Sapota, T., Aldahan, A., Possnert, G., 2006. Be isotopes with textural and mineralogical data of sediment from Lake Baikal (Siberia). Neues Jahrbuch fur Geologie und Palaontologie-Abhandlungen 238, 355–411.
Schaller, M., Lachner, J., Christl, M., Maden, C., Spassov, N., Ilg, A., Böhme, M., 2015. Authigenic Be as a tool to date river terrace sediments?–An example from a Late Miocene hominid locality in Bulgaria. Quat. Geochronol. 29, 6–15.
Singleton, A.A., Schmidt, A.H., Bierman, P.R., Rood, D.H., Neilson, T.B., Greene, E.S., Bower, J.A., Perdrial, N., 2017. Effects of grain size, mineralogy, and acid-extractable grain coatings on the distribution of the fallout radionuclides ^{7}Be, ^{10}Be, 137Cs, and 210Pb in river sediment. Geochem. Cosmochim. Acta 197, 71–86.
Spencer, C.J., Yakymchuk, C., Ghaznavi, M., 2017. Visualising data distributions with kernel density estimation and reduced chi-squared statistic. Geosci. Front. 8, 1247–1252.
Šujan, M., Aherwar, K., Vojtko, R., Braucher, R., Šarinová, K., Chyba, A., Hók, J., Grizelj, A., Pipík, R., Lalinská-Voleková, B., 2023a. Application of the authigenic $^{10}Be/^{9}Be$ dating to constrain the age of a long-lived lake and its regression in an isolated intermontane basin: the case of Late Miocene Lake Turiec, Western Carpathians. Palaeogeogr. Palaeoclimatol. Palaeoecol. 628, 111746.
Šujan, M., Braucher, R., Chyba, A., Vlačiky, M., Aherwar, K., Rózsová, B., Fordinál, K., Maglay, J., Nagy, A., Moravcová, M., 2023b. Mud redeposition during river incision as a factor affecting authigenic $^{10}Be/^{9}Be$ dating: early Pleistocene large mammal fossil-bearing site Nová Vieska, eastern Danube Basin. J. Quat. Sci. 38, 347–364.
Šujan, M., Braucher, R., Kováč, M., Bourlès, D.L., Rybár, S., Guillou, V., Hudáčková, N., 2016. Application of the authigenic $^{10}Be/^{9}Be$ dating method to late miocene–pliocene sequences in the northern danube basin (pannonian basin system): confirmation of heterochronous evolution of sedimentary environments. Global Planet. Change 137, 35–53.
Šujan, M., Braucher, R., Tibenský, M., Fordinál, K., Rybár, S., Kováč, M., 2020. Effects of spatially variable accommodation rate on channel belt distribution in an alluvial sequence: authigenic $^{10}Be/^{9}Be$-based Bayesian age-depth models applied to the upper Miocene Volkovce Fm.(northern Pannonian Basin System, Slovakia). Sediment. Geol. 397, 105566.
Šujan, M., Aherwar, K., Chyba, A., Rózsová, B., Braucher, R., Šujan, M., Šipka, F., 2024. Sedimentological and geochronological data for the fan deltaic nemčiňany formation, upper Miocene. Danube Basin (Slovakia). https://doi.org/10.17632/svr45t2xtj.2. Mendeley Data, V2.
Tan, S.H., Horlick, G., 1987. Matrix-effect observations in inductively coupled plasma mass spectrometry. J. Anal. Atomic Spectrom. 2, 745–763.
Tsai, H., Maejima, Y., Hseu, Z.-Y., 2008. Meteoric ^{10}Be dating of highly weathered soils from fluvial terraces in Taiwan. Quat. Int. 188, 185–196.
Van Wagoner, J.C., Mitchum, R.M., Campion, K.M., Rahmanian, V.D., 1990. Siliciclastic Sequence Stratigraphy in Well Logs, Cores, and Outcrops: Concepts for High-Resolution Correlation of Time and Facies.
Van Wagoner, J.C., Posamentier, H.W., Mitchum, R.M., Vail, P.R., Sarg, J.F., Loutit, T., Hardenbol, J., 1988. An Overview of the Fundamentals of Sequence Stratigraphy and Key Definitions.
Vannoli, P., Burrato, P., Valensise, G., 2015. The seismotectonics of the Po Plain (northern Italy): tectonic diversity in a blind faulting domain. Pure Appl. Geophys. 172, 1105–1142.
von Blanckenburg, F., Bouchez, J., 2014. River fluxes to the sea from the ocean's $^{10}Be/^{9}Be$ ratio. Earth Planet Sci. Lett. 387, 34–43.
von Blanckenburg, F., Bouchez, J., Wittmann, H., 2012. Earth surface erosion and weathering from the $^{10}Be_{(meteoric)}/^{9}Be$ ratio. Earth Planet Sci. Lett. 351–352, 295–305.
Walpole, R.E., Myers, R.H., Myers, S.L., 2012. Probability and Statistics for Engineers and Scientists, ninth ed. Prentice Hall International: Pearson.

Willenbring, J.K., von Blanckenburg, F., 2010. Meteoric cosmogenic Beryllium-10 adsorbed to river sediment and soil: applications for Earth-surface dynamics. Earth Sci. Rev. 98, 105–122.
Wittmann, H., von Blanckenburg, F., Bouchez, J., Dannhaus, N., Naumann, R., Christl, M., Gaillardet, J., 2012. The dependence of meteoric ^{10}Be concentrations on particle size in Amazon River bed sediment and the extraction of reactive $^{10}Be/^{9}Be$ ratios. Chem. Geol. 318, 126–138.
Wittmann, H., von Blanckenburg, F., Mohtadi, M., Christl, M., Bernhardt, A., 2017. The competition between coastal trace metal fluxes and oceanic mixing from the $^{10}Be/^{9}Be$ ratio: implications for sedimentary records. Geophys. Res. Lett. 44, 8443–8452.